



Gondola For High Altitude Planetary Science (GHAPS) Guide System Trade Study

*Michael Lewis, Jeffrey Juergens, and Eliot Aretskin-Hariton
Glenn Research Center, Cleveland, Ohio*

*Robert Woodruff
Robert Woodruff Consulting, Boulder, Colorado*

NASA STI Program . . . in Profile

Since its founding, NASA has been dedicated to the advancement of aeronautics and space science. The NASA Scientific and Technical Information (STI) Program plays a key part in helping NASA maintain this important role.

The NASA STI Program operates under the auspices of the Agency Chief Information Officer. It collects, organizes, provides for archiving, and disseminates NASA's STI. The NASA STI Program provides access to the NASA Technical Report Server—Registered (NTRS Reg) and NASA Technical Report Server—Public (NTRS) thus providing one of the largest collections of aeronautical and space science STI in the world. Results are published in both non-NASA channels and by NASA in the NASA STI Report Series, which includes the following report types:

- TECHNICAL PUBLICATION. Reports of completed research or a major significant phase of research that present the results of NASA programs and include extensive data or theoretical analysis. Includes compilations of significant scientific and technical data and information deemed to be of continuing reference value. NASA counter-part of peer-reviewed formal professional papers, but has less stringent limitations on manuscript length and extent of graphic presentations.
- TECHNICAL MEMORANDUM. Scientific and technical findings that are preliminary or of specialized interest, e.g., “quick-release” reports, working papers, and bibliographies that contain minimal annotation. Does not contain extensive analysis.
- CONTRACTOR REPORT. Scientific and technical findings by NASA-sponsored contractors and grantees.
- CONFERENCE PUBLICATION. Collected papers from scientific and technical conferences, symposia, seminars, or other meetings sponsored or co-sponsored by NASA.
- SPECIAL PUBLICATION. Scientific, technical, or historical information from NASA programs, projects, and missions, often concerned with subjects having substantial public interest.
- TECHNICAL TRANSLATION. English-language translations of foreign scientific and technical material pertinent to NASA's mission.

For more information about the NASA STI program, see the following:

- Access the NASA STI program home page at <http://www.sti.nasa.gov>
- E-mail your question to help@sti.nasa.gov
- Fax your question to the NASA STI Information Desk at 757-864-6500
- Telephone the NASA STI Information Desk at 757-864-9658
- Write to:
NASA STI Program
Mail Stop 148
NASA Langley Research Center
Hampton, VA 23681-2199

NASA/TM—2020-220490



Gondola For High Altitude Planetary Science (GHAPS) Guide System Trade Study

*Michael Lewis, Jeffrey Juergens, and Eliot Aretskin-Hariton
Glenn Research Center, Cleveland, Ohio*

*Robert Woodruff
Robert Woodruff Consulting, Boulder, Colorado*

National Aeronautics and
Space Administration

Glenn Research Center
Cleveland, Ohio 44135

May 2020

This report contains preliminary findings,
subject to revision as analysis proceeds.

Trade names and trademarks are used in this report for identification
only. Their usage does not constitute an official endorsement,
either expressed or implied, by the National Aeronautics and
Space Administration.

Level of Review: This material has been technically reviewed by technical management.

Available from

NASA STI Program
Mail Stop 148
NASA Langley Research Center
Hampton, VA 23681-2199

National Technical Information Service
5285 Port Royal Road
Springfield, VA 22161
703-605-6000

This report is available in electronic form at <http://www.sti.nasa.gov/> and <http://ntrs.nasa.gov/>

Gondola For High Altitude Planetary Science (GHAPS) Guide System Trade Study

Michael Lewis, Jeffrey Juergens, and Eliot Aretskin-Hariton
National Aeronautics and Space Administration
Glenn Research Center
Cleveland, Ohio 44135

Robert Woodruff
Robert Woodruff Consulting
Boulder, Colorado 80304

Abstract

The Gondola for High-Altitude Planetary Science (GHAPS) project is a balloon-borne astronomical observatory designed to operate in the ultraviolet, Visible, and near-mid infrared spectral region. The GHAPS Optical Telescope Assembly (OTA) is designed around a 1-m aperture narrow field-of-view telescope with near-diffraction-limited performance. GHAPS will utilize Wallops Arc-Second Pointing System (WASP) for pointing the OTA with an accuracy of 1 arcsec or better. WASP relies heavily on a self-contained star tracker assembly to determine the OTA line of sight. Preliminary structural analysis indicates that potential misalignments could be present between the OTA line of sight and the star tracker FOV center during the expected flight conditions that could compromise GHAPS pointing accuracy.

In response the GHAPS project undertook a trade study to resolve the following issues: (1) estimate the worst case long-term (or bias) pointing misalignments for the GHAPS opto-mechanical configuration, (2) examine the need for additional hardware to correct pointing errors, and (3) determine the best hardware and software implementation to do so. Quantitative comparisons of performance and qualitative estimates of other factors such as mass, volume, power consumption, and cost are combined into an overall assessment of potential solutions. Results are discussed and a recommended implementation is given that is optimized to best achieve pointing performance goals, while minimizing impact to the design, cost, and resources of the GHAPS project.

1.0 Introduction

The Gondola for High-Altitude Planetary Science (GHAPS) project is a balloon-borne astronomical observatory designed to answer critical questions identified in NASA's Planetary Science Decadal Survey. GHAPS builds on previous balloon missions, expanding the offering for planetary scientists to include highly capable long duration missions. GHAPS is designed for

a minimum of five flights, each up to 100 days in duration, minimizing maintenance between flights. A competitive process will be used to select investigators based primarily on proposed science.

GHAPS optical performance will be optimized for observations in the 300 nm to 5 μm wavelength region covering ultraviolet (UV), visible, and near-mid infrared (IR). GHAPS is being designed around a 1-m aperture narrow-field-of-view telescope with a sub-arc second pointing accuracy. Utilizing NASA's stratospheric balloon capabilities, GHAPS will fly at altitudes between 30 to 40 km where astrophysical and planetary observations can be made above more than 99.5 percent of Earth's atmospheric water vapor and other atmospheric disturbances.

The GHAPS Gondola includes the Optical Telescope Assembly (OTA), the Wallops Arc-Second Pointing System (WASP), avionics, thermal, power system, and the Gondola structure and software. Figure 1 shows the current GHAPS Gondola Assembly.

The primary structure and the subsystems are required to be strong and capable of being disassembled for transport, survive landing, and light-weighted to the extent possible to allow for highly capable long duration flights.

1.1 Trade Study Background

GHAPS will utilize the WASP pointing system that combines the information from multiple sensors, including a high precision star tracker, which is primarily responsible for achieving the desired pointing accuracy of 1 arcsec or better. The star tracker is mounted outboard of GHAPS OTA and utilizes its own lens system and image sensor. Preliminary analysis of the OTA stiffness revealed that a potential misalignment between OTA line-of sight (LOS) and star tracker LOS could arise due to diurnal thermal effects and OTA gravity-induced deflection over the range of possible elevation angles. This misalignment has the potential to significantly offset (also referred to as bias offset) the OTA's FOV with respect to the desired science target FOV, as directed by the WASP pointing system.

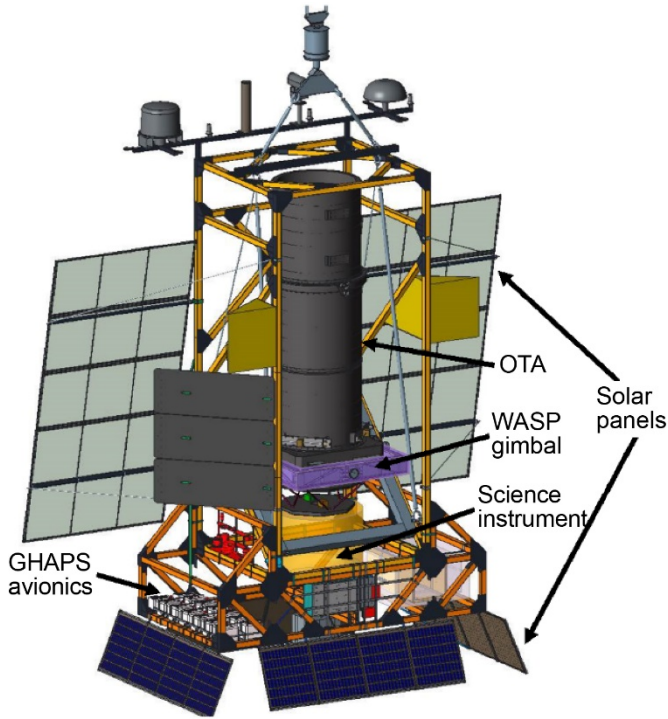


Figure 1.—GHAPS Gondola Assembly Concept.

As a result, the project initiated a trade study to address the following questions:

1. Determine worst-case long-term (bias) misalignments that could develop between OTA LOS and WASP/Star tracker LOS.
2. Determine if additional hardware is needed to reduce this misalignment to comply with the project goal of lower than 1 arcsec pointing accuracy.
3. If additional hardware capability is needed, determine the best implementation for GHAPS.

2.0 Worst Case OTA and Star Tracker Misalignment

At the onset of the trade study, the best information on thermal and gravity deflections of the OTA was found in the OTA Preliminary Design Review data package. The package contained estimated deflections of the primary and secondary mirrors as a function of elevation angle and thermal conditions. Using decenter and tip/tilt sensitivities derived from the optical model of the GHAPS OTA, deflections were then incorporated into a simple model that converted the OTA primary and secondary deflections into changes in LOS. The result is shown in Figure 2 for elevation-induced misalignment and thermal effects are shown in Figure 3.

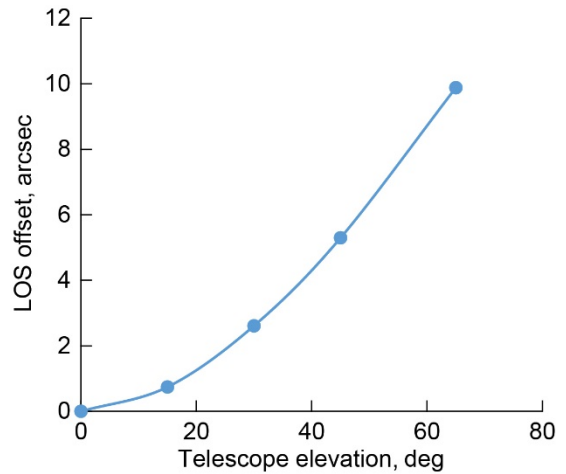


Figure 2.—Worst case OTA gravity induced LOS bias error.

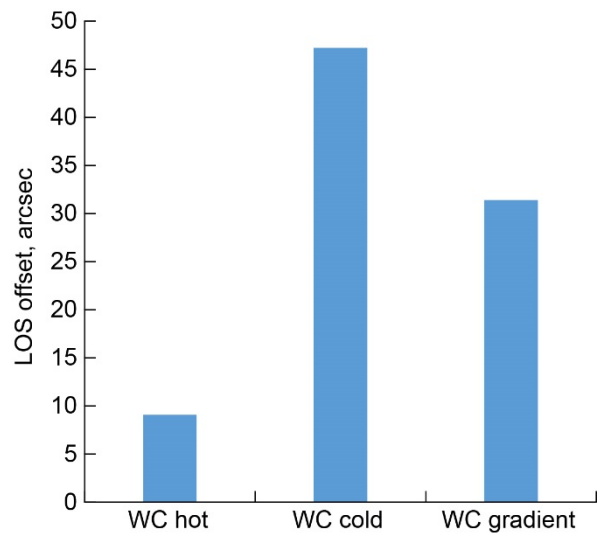


Figure 3.—Worst case thermal induced bias error.

As is evident, the worst-case misalignment is well beyond the 1 arcsec desired pointing accuracy. This estimate does not include deflections and misalignment that the Star tracker and lens will undergo in the same conditions. For the purpose of this worst-case analysis, the star tracker is assumed to be a rigid body whose LOS is unaffected by either elevation angle or thermal environment.

Ground-based OTA and Star tracker boresight alignment can be performed at a median position, both thermally and in terms of elevation angle, which reduces the LOS misalignment with respect to the OTA's average LOS, but maximum LOS excursions are still well above the 1 arcsec goal. More elaborate calibration schemes were examined where the OTA and Star tracker misalignment are characterized at intervals over the entire range of telescope elevations and thermal environments.

Ultimately, this approach was deemed too costly in terms of resources, facilities, and schedule by the project. A simpler, lower resource, alternative would be to add LOS offset detection to the OTA in the form of an OTA guide camera. This camera would reside near the OTA focal plane and image a portion of the OTA FOV. Using stars detected in the OTA Guide Camera FOV, the OTA FOV center in celestial coordinates can be determined to a very high accuracy. The OTA FOV center coordinates can then be provided to the WASP pointing system to properly offset LOS misalignments between Star Tracker and the OTA.

At this stage of the trade study, the worst-case LOS misalignments between OTA and Star Tracker LOS had been shown to significantly exceed the pointing accuracy goals, and it appears that the best approach to solving the issue will require additional OTA capability in the form of a Facility Guide Camera dedicated to detecting the OTA LOS.

At a later point in the trade study, a more refined analysis of the OTA pointing performance was presented which showed marked improvement in gravity and thermal induced pointing errors. Results are shown in Figure 4. The maximum in-flight pointing error due to gravity is approximately 6.0 arcsec. Similarly, the thermal effects are expected to be less than 2.0 arcsec/hr. Although the most recent estimates are much better in terms of maximum expected bias error, the analysis still assumes perfect mechanical joints and material properties. Perhaps additional design iterations could improve pointing further, but until it can be shown, with margin, in a high fidelity model, the project should proceed assuming some form of pointing bias measurement and correction is needed.

3.0 Facility Guide Camera Trade

Many factors will influence the optimum guide camera implementation, however in all cases the camera will need to image very faint stars with an acceptable signal to noise ratio, due to the relatively small FOV that it can utilize. Figure 5 shows the relevant FOVs enabled by the GHAPS overall configuration when incorporating a guide camera. The Wave Front Sensor (WFS) is a separate system that is used by GHAPS to reduce OTA wave front error in flight, and this portion of the FOV cannot be utilized by the guide camera. The Science FOV is area of the OTA focal plane that most Science Instruments are expected to utilize, and cannot be used by the Facility Guide System (FGS) as well. Therefore, the maximum FOV available to the FGS is the OTA's full 450 arcsec diameter FOV minus the Science FOV, and minus the WFS FOV.

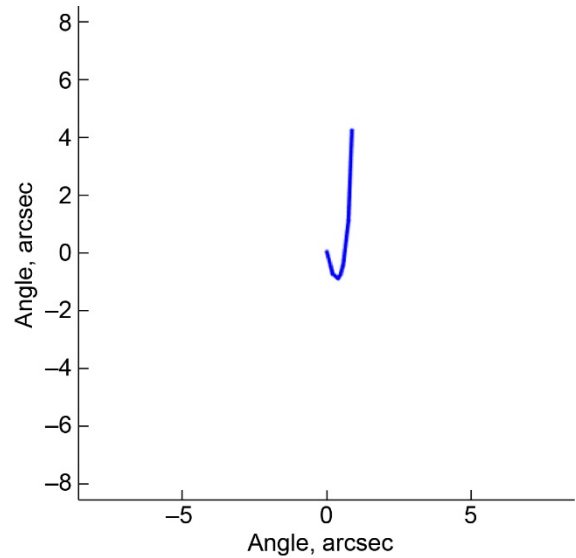


Figure 4.—Migration of on-axis focal spot with elevation. OTA gravity induced pointing errors over full elevation range.

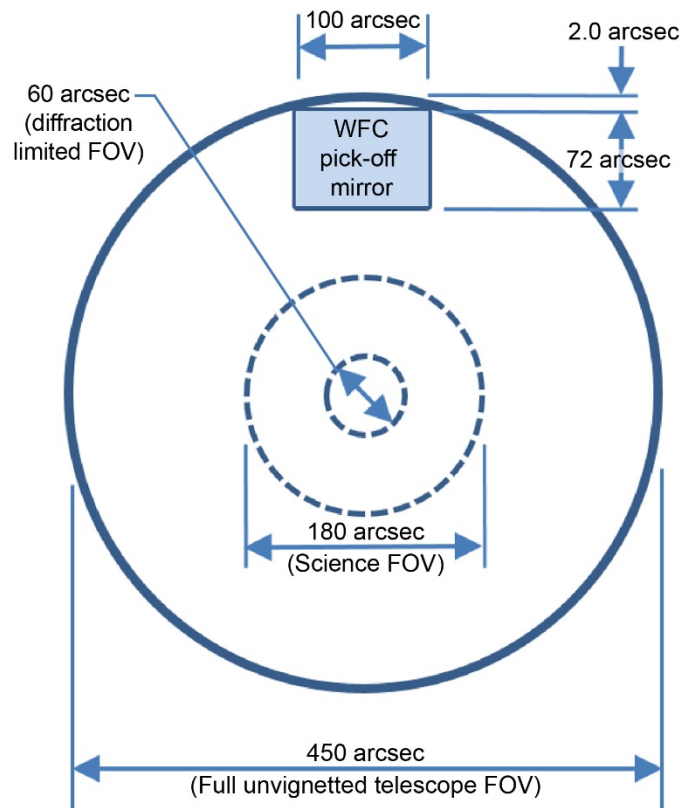


Figure 5.—GHAPS OTA FOV at Cassegrain focus.

3.1 Photometry

As is apparent from the small FOV available to the FGS, it will need the capability to image relatively dim stars (approx. > visible magnitude 16) for a high probability of even a single star capture over any random section of the entire sky. To adequately predict the FGS limiting star magnitude a first order photometric model was developed that included the GHAPS OTA, sky background, star radiance, FGS Image Sensor, and any reimaging optics that may be needed.

3.1.1 Image Sensors

The GHAPS OTA design goal is for nearly diffraction-limited image quality from visible to mid-IR (0.5 to 5 μm). Potential FGS image sensors could operate anywhere in this spectral range. For the trade study, the following types of image sensor technologies were examined in terms of performance:

1. Scientific CMOS (sCMOS)
2. Depletion CCD (D-CCD)
3. InGaAs
4. HgCdTe
5. InSb
6. e-APD (HgCdTe)

Both image sensor and camera performance data were obtained from various manufactures, and candidates with the best compromise in sensitivity, noise, size, weight, and power was chosen for each technology.

Table 1 shows the relevant characteristics for each of the sensor technologies. A number of the sensor technologies require closed cycle sterling coolers (cryocooler) to achieve good noise figures. Cryocoolers add mass, volume, and power consumption compared to devices that only require thermoelectric cooling (TE). The GHAPS OTA and Instrument Bay will be susceptible to random and sinusoidal vibration, which is

inherent with all cryocooler devices, hence image sensor technologies that require a cryocooler were removed from further consideration.

Depletion-CCD (D-CCD) technology does not require a cryocooler, however there are other operational characteristics that can make it less desirable. D-CCD devices are standard CCD structures that are first back thinned and have an addition layer of silicon added which tunes their spectral response toward the longer wavelengths, compared to bulk silicon spectral response. This process opens the device up to interference filter-like effects due to the differences in index of refraction. The resulting effect is a periodic sinusoidal fringe pattern in the background (dark frame) that can be substantial compared to other noise mechanisms. An antireflective coating can reduce much of this effect, but cannot remove it completely. In addition, all integrated cameras that could be equipped with D-CCD images sensor provide a single tap video output, which severely limits the maximum full frame rate that the unit can generate. For these reasons, D-CCD technology was also eliminated from further consideration. The detailed photometric analysis concentrated on only sCMOS and InGaAs image sensor technologies.

3.1.2 Star Radiance

Star spectral radiance was approximated using a black-body spectral radiance equation from Zombeck (Ref. 1).

$$L(\lambda) = \frac{8.48 * 10^{34} * 10^{(-0.4*m_b)}}{T_e^4 \lambda^4 [e^{(1.44 * \frac{10^8}{\lambda T_e})} - 1]} \text{ Photons cm}^{-2} \text{ s}^{-1} \text{ A}^{-1}$$

where T_e is the effective black body temperature of the star. For initial calculations an effective temperature of 5,780 K was used, which relates closely to Main Sequence stars of Class G0 in the Hertzsprung-Russell diagram. λ is the wavelength of light in Angstroms. m_b is the bolometric magnitude of the star, which is derived from its visible magnitude with a bolometric

TABLE 1.—FGS IMAGE SENSOR TECHNOLOGIES

Sensor	QE/Band	Size	Noise	Camera manufacturer	Physical
sCMOS	80-95% peak (0.4-1.0 μm) Peak at 0.6 μm	Up to 4,000 by 4,000 Pixel: 4.5-13 μm	Excellent	Photometric Andor, Ximea Raptor, etc.	TE cooled (-20 to -50 °C) Small Size
Depletion-CCD	70-95% peak (0.5-1.0 μm) Peak at 0.8 μm	Up to 1,000 by 1,000 Pixel: 13-20 μm	Good	Princeton Imaging, FLI	TE cooled (-60 °C) Small size
InGaAs	80-90% peak (0.5-1.7 μm) Peak at 1.2 μm	Up to 1,000 by 1,000 Pixel: 13-20 μm	Good-Fair	PI, FLIR, IR Cameras, Raptor, etc.	TE cooled (-20 to -50 °C) Small to medium size
HgCdTe (MCT)	80-90% peak (1.6-5.3 μm) Custom peak	Up to 4,000 by 4,000 Pixel: 10-18 μm	Good	Low Res- FLIR High Res - Teledyne	Sterling Cooler (120 to 77 K) Larger size
A-MCT	70% QE peak (1.1-2.5 μm)	320 by 256 Pixel: 24 μm	Excellent	First Light, Imaging, Selex, Voxel	Sterling Cooler (77 K) Larger size
InSb	80-90% peak (1-5.5 μm) Flat	Up to 1,000 by 1,000 Pixel: 12-20 μm	Good-Fair	FLIR, L3, Raytheon	Sterling Cooler (77 K) Larger size

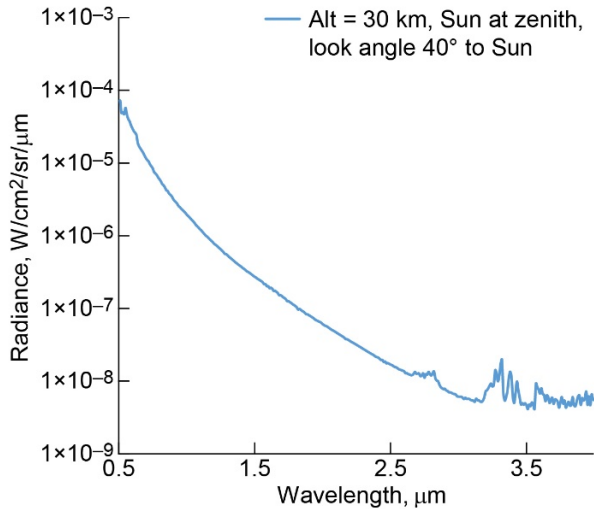


Figure 6.—GHAPS worst case daytime sky radiance—MODTRAN only.

correction factor to compensate for radiance outside the visible range. Bolometric correction factors were obtained from recent work by Pecaut and Mamajek, 2013 (Ref. 2). An even more up to date version is available on line at following site: (http://www.pas.rochester.edu/~emamajek/EEM_dwarf_UBVII_HK_colors_Teff.txt)

3.1.3 Sky Background

GHAPS has requirements to make scientific observations during both night and daytime, therefore the FGS must capture star(s) in both daytime and night for LOS bias offset to be determined. Sky background for nighttime operation is generally not a limiting factor in guide cameras as the typical night sky radiance is lower than visible magnitude 22 per square arcsec. In daytime operation, the sky background usually becomes the most significant factor for limiting magnitude star detection.

GHAPS will operate at an altitude of approximately 30 km, which puts the OTA above a large portion of the atmosphere that scatters daytime sunlight. As such, the daytime sky background irradiance will be significantly lower than the background seen by land-based telescopes (Ref. 3). An accurate model of the daytime sky background is needed to properly evaluate the various types of images sensors and their possible windows of operation in the optical spectrum. The MODTRAN6 software simulation package from Spectral Sciences Inc. was used to simulate worst-case daytime sky background spectral irradiance levels at 30 km, including the worst sun angle and OTA look angles. The expected daytime spectral radiance shown in Figure 6 is limited to a range from visible to 4 μm since sky radiance increases abruptly by 3 to 4 orders of magnitude beyond 4.2 μm. Good agreement is seen in the plot when compared to similar literature on daytime

atmospheric radiance, including the GHAPS Science Instrument Definition Team (SIDT) Report (Ref. 4).

3.1.3.1 Air Glow Emissions

The MODTRAN simulation package is capable of only modeling radiation transport through the Earth’s atmosphere using known radiative sources. It cannot predict the simulated emission of electromagnetic radiation that takes place in the Earth’s upper atmosphere in either daytime or night. Of particular interest is the known bands of emission that occur in the near IR referred to as airglow. Airglow is caused by various processes in the upper atmosphere such as luminescence by cosmic rays, recombination of solar photoionized atoms, and chemiluminescence from reactions between upper atmospheric molecules. Nighttime airglow spectral radiance is well documented, however little quantitative data on daytime values is available at the altitudes in which GHAPS will be observing.

An estimation of daytime spectral radiance was performed using data obtained from the SABER instrument (Sounding of the Atmosphere using Broadband Emission Radiometry) which is operated aboard the TIMED satellite (Thermosphere Ionosphere Mesosphere Energetics Dynamics). SABER is a radiometric instrument that scans the Earth’s atmospheric limb, its apparent visual edge, from 0 to over 120 km multiple times as it orbits. SABER generates radiance measurements at several specific bands in the near to mid IR (1.25 μm - O₂, 1.6 μm - OH, and 2.0 - OH) (Ref. 5). Based on the literature (Ref. 6), it appears that airglow intensity can be assumed to scale linearly across the near IR spectra, i.e. the relative intensity from emission line to emission line remain approximately the same as the overall intensity increases in daytime versus night. With this assumption, the SABER data can be used to obtain a night time to daytime correction factor that can be applied to the well know nighttime airglow spectra.

Figure 7 shows a typical plot of the SABER dataset in the bands of interest. Based on an arbitrary 7-day average, the worst-case daytime to night airglow ratios appear to be approximately 100. This estimate is relatively conservative and incorporates the subtraction of daytime MODTRAN sky radiance from the raw SABER data. Detailed nighttime airglow spectra was obtained from measurements taken at European Southern Observatory’s (ESO) Very Large Telescope (VLT) at Cerro Paranal (Ref. 7). ESO provides an online tool to calculate nighttime airglow at look angles from 19.5° to zenith. Airglow nighttime spectra with a look angle of 19.5° was used, as this is closer to the worst case GHAPS look angles for airglow. Figure 8 shows the MODTRAN computed daytime sky irradiance with the superimposed daytime airglow estimate. At certain wavelengths longer than 1 μm, the daytime airglow exceeds the MODTRAN radiance estimates, which will significantly impact the overall performance of near IR image sensors.

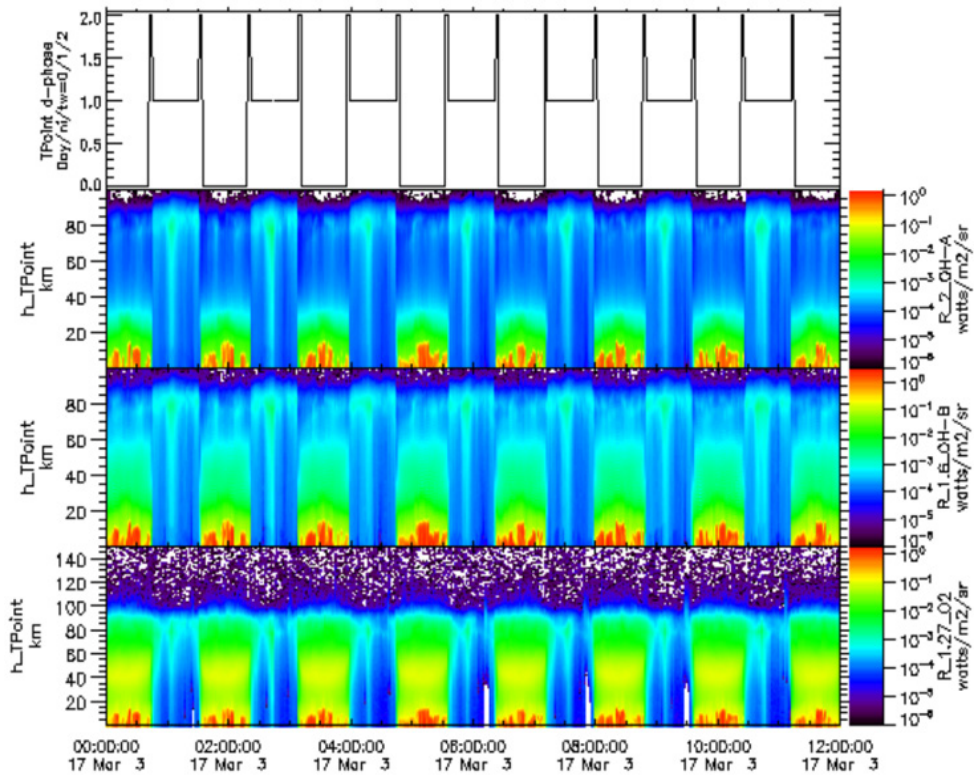


Figure 7.—Typical SABER radiance data.

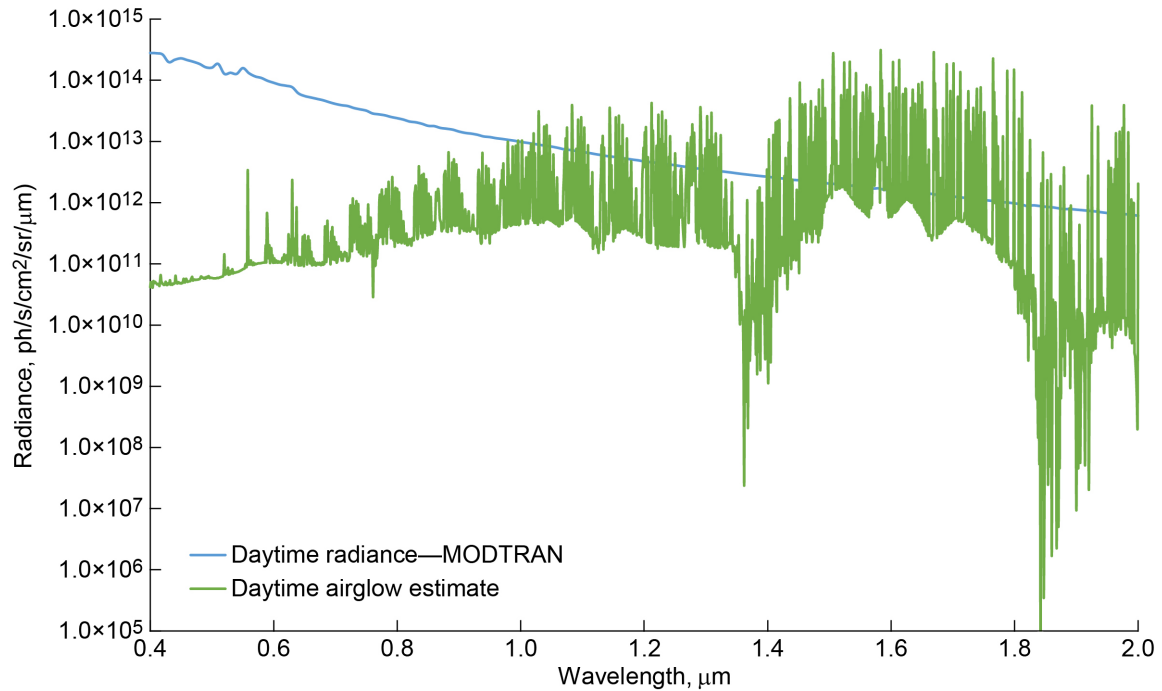


Figure 8.—Daytime sky radiance components—30 km, Sun at zenith, 20° look angle.

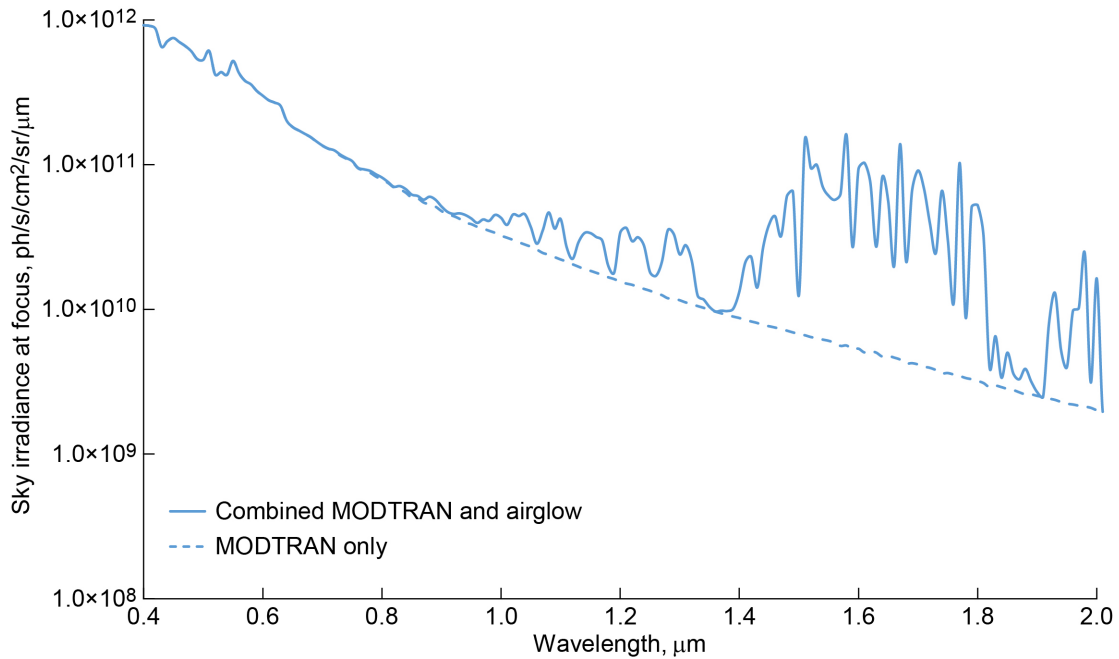


Figure 9.—Composite enveloped worst case sky irradiance at Cassegrain focus for GHAPS photometric model.

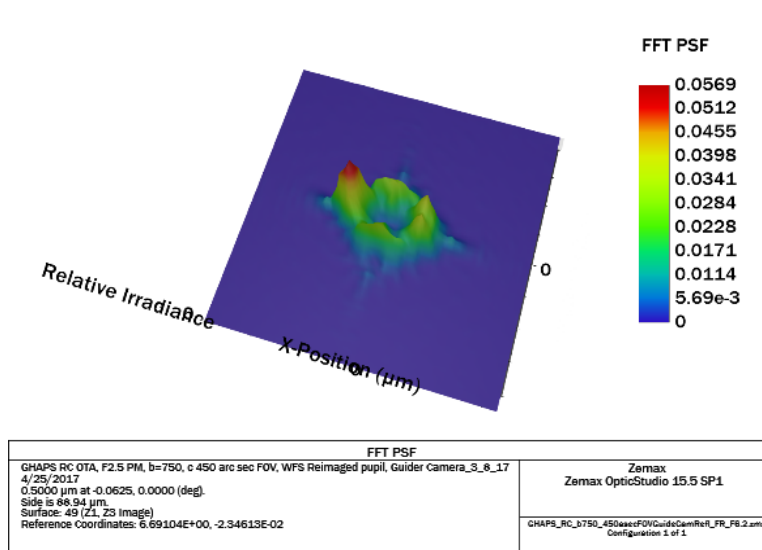


Figure 10.—Typical reimaging optics PSF performance.

Figure 9 shows the combined MODTRAN and daytime airglow irradiance at Cassegrain focus in an enveloped form that will be used for calculating each candidate image sensor’s performance as a potential device for the FSG.

3.1.4 Reimaging Optics

All image sensors being considered for the FGS have an active area that is smaller than the telescope FOV at Cassegrain focus. The probability for star detection in a random sky FOV

is proportional to the limiting magnitude of the FGS and its FOV. To maximize star detection probability, a demagnification of the telescope FOV is needed. Optical models were generated for a two-mirror Korsch and commercially available refractive focal reducers, using design parameters that map the OTA FOV to the full size of a single FGS candidate image sensor. Results showed that all optical models significantly aberrated the ideal PSF to such an extent that limiting magnitude was made significantly worse. Figure 10 shows a typical PSF for one of the two-mirror Korsch designs.

With these results, the recommendation was to forgo any FGS reimaging optic, and simply place FGS image sensor at telescope Cassegrain focus. FGS optics will consist only of a pick-off mirror and band pass filter. The implication of this design choice is that multiple image sensors and/or cameras may be needed to image enough of the telescope FOV to assure reliable star detection within any random sky section.

3.1.5 OTA Photometry

For this first order photometry model, the OTA is represented by an idealized 1-m diameter Ritchey-Chrétien telescope with F/# ratio of 14.052, and a central obscuration of 10 percent by area. Transforming sky radiance to focal plane irradiance was done using the optical étendue relationship with the form below:

$$E_{sky @ focus} = \frac{L_{sky} \pi}{4 (F\#^2)} * Scope Trans$$

(Where Scope Transmission = 0.82)

Telescope transmission is approximated by multiplying the reflectivity of primary and secondary mirrors with the fractional unobstructed aperture ($T_{scope} = R_{M1} * R_{M2} * 0.9 = 0.82$, where $R_{M1} = R_{M2} = 0.96$).

Star radiance is transformed into focal plane irradiance by assuming diffraction limited performance, in which all light that

is captured by the OTA aperture is concentrated into a single point spread function (PSF) of diffraction limited shape at the focal plane. As is the case for sky background, star radiance is also multiplied by scope transmission. For analysis purposes, a conservative estimate of the imaged star spot size was used. Instead of the usual diffraction limited FWHM, the radius of the first minimum is used, $r_{Airy disk} = 1.22\lambda/d$, where d is the diameter of the OTA aperture.

In addition to the computations listed above, an adjustable band pass filter was added to the model so that each sensor could be optimized for the best spectral pass band from visible to the mid IR. In all cases, the filter was modeled as an idealized step function at turn on and turn off wavelengths with a 90 percent transmission over the band.

3.1.6 Signal to Noise Ratio (SNR)

Signal to noise ratio for star images against the sky background will determine the reliable detectability of stars and ultimately the ability of the FGS to determine OTA to Star tracker offset. For the purposes of this analysis, a minimum SNR of 10 has been used. This is a relatively conservative threshold, considering that the WASP pointing system star tracker uses a minimum SNR of approximately 7. The effective SNR was calculated using the following formula:

$$SNR_{Star} = \frac{Signal}{Noise} = \frac{QE * Star_{ph Airy disk}}{\sqrt{QE Star_{ph Airy Disk} + n QE Sky_{ph/pixel} + n Dark_{noise} + n (Read_{Noise})^2}}$$

where,

$Star_{ph Airy disk}$ = Total Photons in the Star Airy Disk for the specific Integration Time

$Sky_{ph/pixel}$ = Sky Background $\frac{Photons}{pixel}$ for the specific Image Sensor and Integration Time

n = number of pixels occupied by the star airy disc, first minima

$Dark_{Noise}$ = Image Sensor Dark Noise in $\frac{e}{pixel * sec}$

$Read_{Noise}$ = Image Sensor Read Noise in $\frac{e}{pixel}$ (rms)

QE = Image Sensor Quantum Efficiency

t = Integration Time

3.1.7 Sensor Pixel Size

Pixel sizes for the image sensor being considered ranged from 4.5 μm to as large as 20 μm^2 . The size of the image sensor will have a significant impact on the average number of signal electrons/pixel that are generated for a particular image sensor. Given the same Airy disk diameter, a smaller pixel sensor will

have fewer photons/pixel as compared to a sensor with larger pixels at the same QE.

Additional consideration must be given to the minimum number of pixels for a star image in order to achieve reliable centroid detection and ultimately a reliable measure of OTA to Star Tracker offset. Based on current star tracker centroiding algorithms, a recommendation of at least nine pixels in area is

needed for accurate and reliable star position. Therefore, the photometric analysis assumes at least nine pixels for the area of the Airy disk first minimum, in a format that places at least three pixels across the Airy diameter. The Airy disk is a function of both telescope diameter and wavelength. The midpoint of the band pass filter for the image sensor was used in estimating the Airy disk diameter. Depending on the pixel size and the band pass filter center wavelength, Airy disk areas could be fewer than nine pixels. In these cases, diameters were increased to at least nine pixels so that the centroiding criteria is met and a more realistic side-by-side comparison is achieved. The implication of a nine pixel Airy disk minimum means that some image sensors with large pixels will require a small amount of defocus to increase the image diameter.

3.1.8 Sensor Integration Time

The WASP system will provide a 1 arcsec pointing accuracy in which the majority of the error manifests itself as jitter about some average LOS in the cross-boresight plane. At the OTA focal plane, the star image will jitter in a similar fashion, which can smear the star image over a larger area. Sensor integration time has a significant impact on detectable limiting star magnitude. Longer integration times create more star signal electrons per pixel, however they also create larger image smear, which spreads out the star signal over more pixels.

In addition to the FGS determining a bias offset between the OTA and WASP star tracker, the FGS has a desired secondary function to estimate focus quality of the OTA. The OTA WFS system is not a continuous correction system. It requires that GHAPS pause from observing the science object and slew the OTA to a bright guide star for wave front sensing and correction. Knowing when to correct the OTA alignment must come from either a predictive analysis or a measure of image quality during observation. Therefore, if the FGS can provide image quality information in addition to its primary functionality, it would provide the means to determine when WFS correction is needed without additional hardware. Bias offset detection relies heavily on centroiding algorithms, which are relatively tolerant of image smear, however image quality algorithms are relatively intolerant of image smear (Ref. 8).

In a parallel effort, an initial examination of possible image quality algorithms was undertaken. They included direct PSF sampling, autocorrelation, and image sharpness measurements. Autocorrelation was chosen for further evaluation since it is expected to perform well even with a small sampling of the PSF (Ref. 9). The accuracy of all these algorithms will be affected by image smear.

In order to preserve the potential for the FGS to measure OTA focus quality, some bounds on integration time are needed. Based on anticipated image quality algorithms, a base-

line of smaller than $\frac{1}{4}$ pixel smear per frame was used. Considering the WASP jitter velocities and minimum pixel size of image sensors candidates is $4.5 \mu\text{m}$, a baseline of 10 ms integration time has been chosen. This is a conservative estimate, as image sensors with larger pixels could have a proportionally larger integration time and still meet the $\frac{1}{4}$ pixel image smear.

3.1.9 Image Sensor Performance

Using the assumptions and approximations given in the previous sections for sky background radiance, star radiance, image sensor parameters, and integration time, the daytime focal plane performance was generated for two commercially available versions of the sCMOS and InGaAs image sensors. Results are shown in Figure 11. In each case, the spectral pass band was optimized for the maximum SNR, and star images were assumed to occupy at least nine pixels in area at the focal plane.

As expected, all image sensors exhibit a slope change when various elements of the SNR dominate the resulting performance. At the brightest star magnitudes, the performance curve flattens due to pixel full well saturation, middle magnitudes are dominated by star shot noise effects, and the dimmest magnitudes are driven by a combination of sky background shot noise and sensor read noise. Using a minimum SNR of 10 as the threshold for FGS tracking algorithms, Figure 11 shows that both sCMOS image sensors give nearly the same performance. The InGaAs image sensors show a marked difference in performance. This can be attributed to the extensive TE cooling and low read noise of InGaAs 2 sensor compared to the InGaAs 1 sensor. (Read noise of 30 electrons/pixel versus 170 electrons/pixel, respectively.)

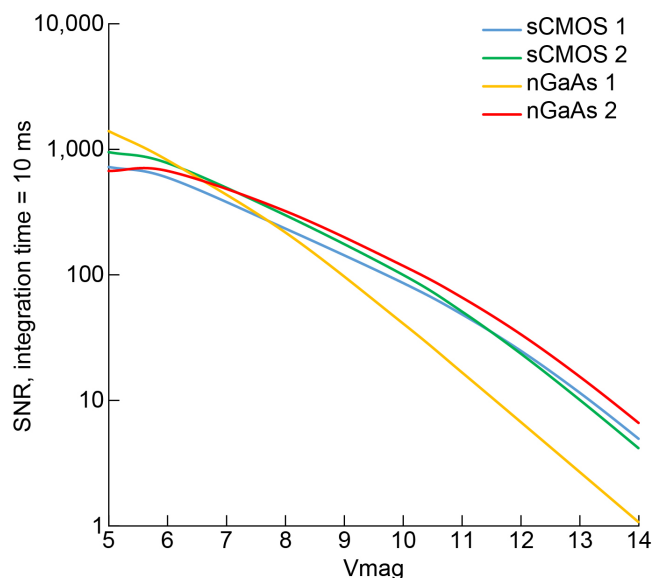


Figure 11.—Image performance comparison—GHAPS worst case daytime, 10 ms integration time.

Class	Effective temperature ^{[1][2][3]}	Vega-relative chromaticity ^{[4][nb 1]}	Main-sequence radius ^{[1][8]} (solar radii)	Main-sequence luminosity ^{[1][8]} (bolometric)	Hydrogen lines	Fraction of all main-sequence stars ^[9]
O	≥ 30,000 K	blue	≥ 6.6 R_{\odot}	≥ 30,000 L_{\odot}	Weak	~0.00003%
B	10,000–30,000 K	blue white	1.8–6.6 R_{\odot}	25–30,000 L_{\odot}	Medium	0.13%
A	7,500–10,000 K	white	1.4–1.8 R_{\odot}	5–25 L_{\odot}	Strong	0.6%
F	6,000–7,500 K	yellow white	1.15–1.4 R_{\odot}	1.5–5 L_{\odot}	Medium	3%
G	5,200–6,000 K	yellow	0.96–1.15 R_{\odot}	0.6–1.5 L_{\odot}	Weak	7.6%
K	3,700–5,200 K	light orange	0.7–0.96 R_{\odot}	0.08–0.6 L_{\odot}	Very weak	12.1%
M	2,400–3,700 K	orange red	≤ 0.7 R_{\odot}	≤ 0.08 L_{\odot}	Very weak	76.45%

Figure 12.—Harvard stellar class distribution of local Milky Way Galaxy stars.

Using an integration time of 10 ms, both sCMOS and InGaAs will have visible limiting magnitude between 13 and 13.5 for stars that can be used to compute the bias offset. The probability of capturing magnitude 13.5 or brighter stars is dependent on the FOV available to the FGS.

At a SNR of 10 the InGaAs 2 sensor has approximately a 0.3 magnitude advantage over the sCMOS sensors. Using information on mean star density as function of visible magnitude from Zombeck (Ref. 1) and the maximum FOV available to the FGS, the InGaAs sensor will capture roughly 1.52 stars in a random sky section versus 1.32 for the best sCMOS sensor, using a 10 ms integration time. It should be noted that the mean star density listed in Zombeck occur at roughly a galactic latitude of 20°. Stellar density drops quickly at latitudes above 20° to the point where less than one star is acquired by the FGS at galactic latitudes higher than 40°. This leaves a large portion of the sky with a low probability of imaging stars for the FGS, and consequently no bias offset measurement capability.

3.1.10 Potential InGaAs Advantage With Star Spectral Radiance

The previous photometric analysis was conducted assuming all stars have the same spectral radiance content, class G0 stars with effective temperature of 5,780 K. The actual sky will have stars with a wide range of effective temperatures. The predicted distribution of effective star temperatures within our galaxy has been well documented (Refs. 10 and 11), and is shown in Figure 12. The majority of stars appear to have relatively low effective temperatures, which places a higher portion of their spectral radiance in the near-IR band. Considering the spectral sensitivity of InGaAs and sCMOS sensors, the possibility exists that InGaAs may have a significantly better detection capability for lower effective temperature stars than sCMOS, ultimately leading to a significantly higher probability for star detection over more of the sky.

The potential spectral advantage of InGaAs was investigated by first utilizing the same photometry model used to determine SNR versus visible magnitude. By varying the range of effective star temperatures in the model and determining the stellar

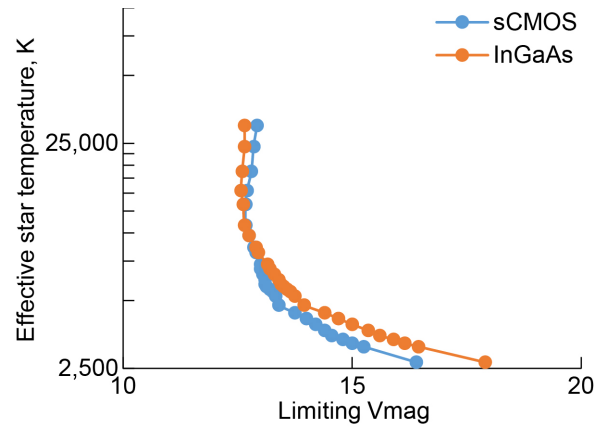


Figure 13.—InGaAs and sCMOS limiting magnitude (SNR>10) as a function of star effective temperature.

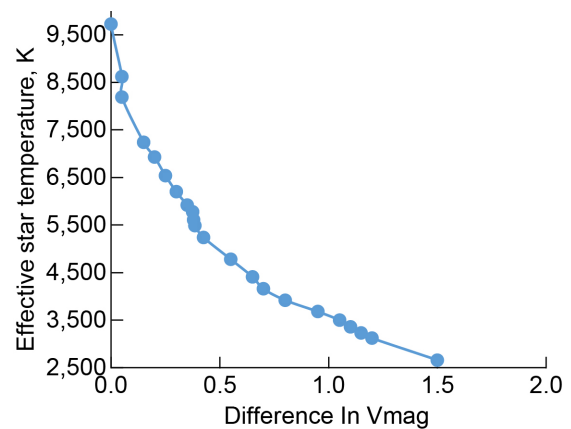


Figure 14.—Limiting magnitude (SNR>10) advantage of InGaAs over sCMOS.

magnitude when SNR equals 10, a curve of each sensor’s limiting magnitude (SNR=10) versus effective star temperature was generated. Figure 13 show the results for sCMOS and InGaAs. Figure 14 show the difference in limiting magnitude performance between InGaAs and sCMOS. The performance difference may seem relatively small, but if the majority of stars have effective temperatures lower than 3,800 K, then InGaAs has an advantage

of over one magnitude compared to sCMOS. This equates to a potential doubling of the star density that can be captured.

Rather than using a predictive estimate of star spectral class distribution, analysis went forward using actual star catalogs that have the capability to reach at least magnitude 17 stars. Several catalogs were considered, but the NOMAD star catalog was chosen due to its combination of star quantity and spectral magnitude at both visible and near IR photometric bands. The NOMAD catalog is a combination of Hipparcos, Tycho-2, UCAC-2, USNO-B1, and 2MASS surveys, and contains over 1 billion star down to visible magnitude 22.

Obtaining and working with the entire NOMAD catalog is difficult and time consuming due to its size. As a compromise, a subsample of the NOMAD catalog was used. Using the NOMAD online search capability, cone search data for many 1° radius fields were obtained. Cone searches were obtained for each galactic latitude in 10° increments and four searches (longitude 0°, 90°, 180°, and 270°) at each galactic latitude. This yielded star sample sizes at each latitude from 16,000 at the poles to more than 180,000 near the equator.

Figure 15 and Figure 16 show relevant statistics for the NOMAD star subset collected at a galactic latitude of 10°. Although the plot of star count versus visible magnitude exhibits the constant log slope as expected, the plot of stellar spectral class count differs significantly from that expected by literature. In both the NOMAD and its subset 2MASS, the fraction of cooler K and M class stars is much lower than expected. This is also consistent with findings from another catalog that was initially considered called APASS. This discrepancy was never fully explained, but it appears that the cataloging of cooler stars may be limited by the inherently lower visible and near IR magnitudes that they possess. As a result, InGaAs sensor will likely not have the significant advantage over sCMOS as first hoped. Nonetheless, a quantitative performance analysis of the two sensors was still carried out using the NOMAD catalog data.

A relationship between photometric bands V, J, and effective star temperature were obtained using data from Pecaut and Mamajek (Ref. 2). For each star, the V-J value was obtained and translated into an effective temperature. The FGS limiting magnitude was generated for each catalog star from the V-J relationship and the curve fit described in Section 3.1.11. Star visible magnitude is then compared to FGS threshold using the star effective temperature. If the star visible magnitude is smaller (brighter) than the FGS threshold, the star can be imaged with a SNR > 10. This was performed for both sCMOS and InGaAs sensors. Predicted FGS star densities at periodic galactic latitudes were then generated by tallying the stars with visible magnitudes brighter than the limiting magnitude of each sensor. Results are shown in Figure 17. True star effective temperature can be affected by three main factors. Star surface gravity, star metallicity, and reddening from interstellar dust.

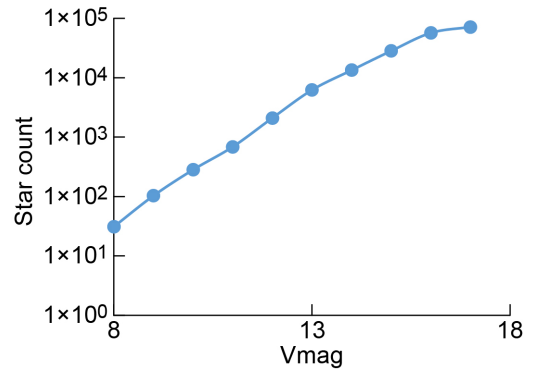


Figure 15.—NOMAD catalog subset star count versus visible magnitude.

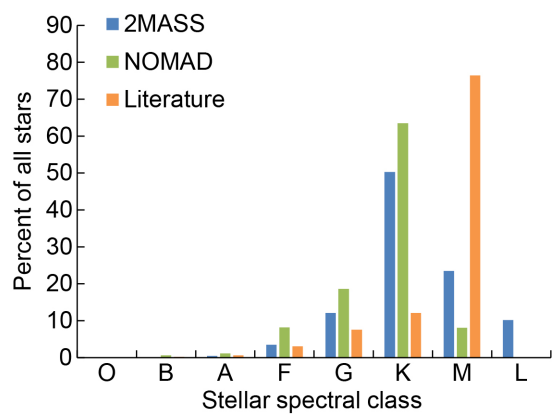


Figure 16.—Stellar spectral class distribution.

Surface gravity and metallicity require detailed spectral scans of the star in question to quantify, so it cannot be applied in this analysis. In lieu of this potential error, these factors were estimated, using information from M.L. Houdashelt, R.A. Bell, 2000 (Ref. 12). The maximum errors were found to be ± 150 K in effective temperature, which relates to approximately ± 8 percent in calculated stellar densities. This level of uncertainty should not significantly affect the results shown in Figure 17.

Results show that InGaAs may have substantial performance gains at lower galactic latitudes, but at latitudes above 50°, the advantage is negligible. Based on Figure 17, InGaAs would be the best choice, however other factors such as size, weight, power, and cost are actually in the favor of sCMOS. Recall that the FGS will not have any reimaging optics to map the maximum telescope FOV to the image sensor. Instead, the image sensor must cover the largest portion possible of the FOV available to it at Cassegrain focus. To do so with InGaAs sensor will require at least three image sensors and cameras. The same may be possible with fewer sCMOS sensors due to their larger array size. The desired functionality of focus quality measurement is also best served by sCMOS arrays versus InGaAs due to their smaller pixel sizes compared to InGaAs arrays. The size and

power consumption of InGaAs is 2 to 3 times that of the sCMOS solution, plus the cost of InGaAs is 3 to 4 times that of sCMOS. For these reasons, sCMOS was chosen as the image sensor technology to implement as an FGS.

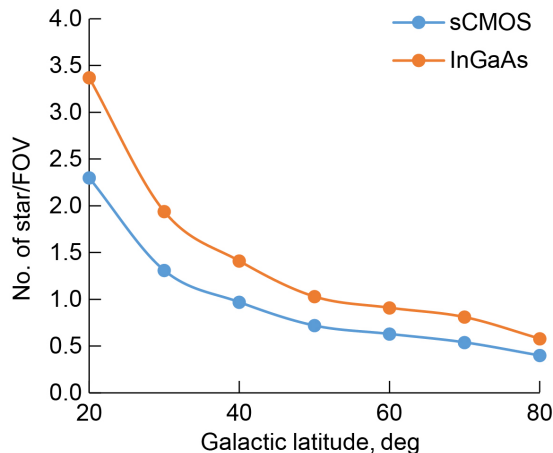


Figure 17.—Predicted FGS star count for InGaAs and sCMOS—10 ms integration time, maximum FGS FOV, optimized spectral passband.

3.1.11 sCMOS Camera Selection

With sCMOS chosen as the best option for the FGS, work began to determine the best sensor and camera(s) for a detailed design implementation. An industry survey was conducted for the best sCMOS camera candidates, which weighed the advantages and disadvantages of many cameras factors. The factors included performance, power, size, weight, cost, etc. A list of candidates is shown in Table 2. The final row of Table 2 shows which candidates had the best compromise between factors to warrant continued development with the FGS. The best sCMOS camera candidates included the following:

1. Finger Lakes Inc., KL400
2. Ximea, CB152MS-GP-X4G2
3. Andor, Zyla 5.5 (Improved QE, 80 percent)

Without any reimaging optics, the FGS must capture as much of the available FOV as possible, which requires multiple cameras in all cases. Figure 18 shows an overlay of the OTA FOV with the best four options of FGS sensor layout using the sCMOS cameras listed above.

TABLE 2.—CANDIDATE SCMOS CAMERA CHARACTERISTICS

	FLI KL400	Nikon DS-2iQ	Ximea CB152MS-GP-X4G2	Andor Zyla 5.5	QHY 163M/ ZWO 1600MM
Sensor	2,048 by 2,048 (22.5 by 22.5 mm)	4,908 by 3,264 (36 by 24 mm)	4,656 by 4,104 (21.8 by 12.6 mm)	2,560 by 2,160 (16.6 by 14 mm)	4,656 by 3,522 (17.7 by 13.4 mm)
Pixel size	11 μm	7.3 μm	4.25 μm	6.5 μm	3.75 μm
Peak QE (%)	95 (at 570 nm)	80 (at 500 nm)	71 (at 570 nm)	80 (at 570 nm)	60 (TBR)
Read noise (RMS)	1.5	2.2	1.4	1.6	1.2
Daytime limiting visible mag. (exp. time, smear)	13.8 (35 ms, 1/2 pix) (3 σ smear)	13.0 (20 ms, 1/2 pix) (3 σ smear)	13.35 (13 ms, 1/2 pix) (3 σ smear)	13.65 (20 ms, 1/2 p) (3 σ smear)	13.0 (10 ms, 1/2 pix) (3 σ smear)
Daytime limiting visible mag.	15.3 (1 sec) (1 σ smear)	14.7 (1 sec) (1 σ smear)	15.15 (1 sec) (1 σ smear)	15.2 (1 sec) (1 σ smear)	
Size (mm)	102 by 102 by 106	105 by 134 by 153	50 by 50 by 55	80 by 80 by 133	100 diam. by 120
Mass (kg)	1.5 (TBR)	1.2	0.17	1.0	0.41
Power	25 W (TBR)	24 W	<16 W	60 / 30 W	24 W
Cost	\$15,000 (TBR)	\$20,000	\$15,000	\$15,000	\$1,200
Software	Windows, Linux	Windows	Windows, Linux	Windows, Linux	Windows, Linux
Multicamera sync	Yes	N/A	Yes (TBR)	Yes	No
Pursue further	Yes, Aug. 2017 release	No	Yes	Yes, 2017 release	No

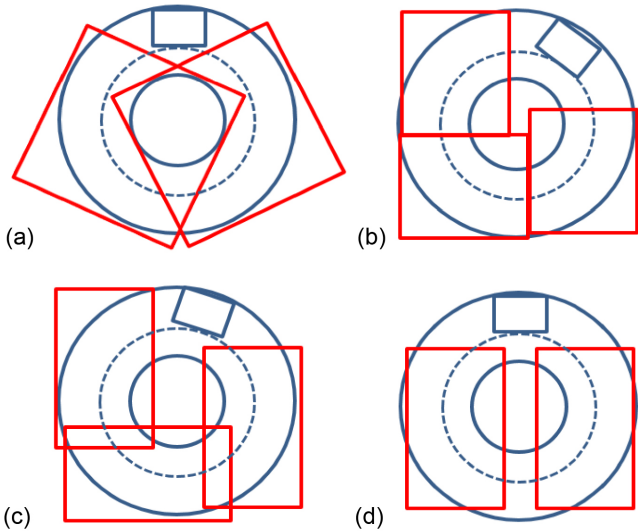


Figure 18.—Image sensor layouts for FGS FOV coverage. (a) FLI KL400 (2x) 8.7×10^4 arcsec². (b) Zyla 5.5 (3x) 7.8×10^4 arcsec². (c) Ximea (3x) 9.1×10^4 arcsec². (d) Ximea (2x) 6.4×10^4 arcsec².

3.1.12 Extended Integration Time

The results in Figure 17 show that even when imaging the maximum available FOV for the FGS, using a 10 ms integration time, neither image sensor technology will be capable of delivering reliable star imaging over the full sky. This leads to a different approach in which significantly longer sensor integration time is needed. As stated earlier, longer integration times allow more star signal photons to accumulate in the pixels contained in the PSF, but that additional time allows jitter to spread out the PSF, which offsets the benefit. To estimate the star image smearing effect, information is needed about the WASP cross-boresight jitter as a function of time. As part of the GHAPS project, a medium fidelity simulation model of the WASP and OTA has been developed. Using simulation data obtained from a typical target angle over a 60-sec period, high resolution pointing jitter data was derived. The results were statistically characterized to obtain jitter velocities that were included into the photometry model. Jitter was characterized as 1σ and 3σ values. One sigma jitter velocity values were used to compensate the photometric model, which is a reasonable value that encompasses > 90 percent of expected jitter during tracking.

Integration time was increased in the model until the image became saturated by the combination of background and star radiance. From that point integration time was reduced approximately 25 percent so that at least four magnitudes of stars could be imaged in a single frame with an SNR > 10 without saturation. This led to an optimized integration time of 2 sec for each image sensor. Using the 2-sec integration time, estimates of stars per FOV were calculated from the model. Results are shown in Figure 19.

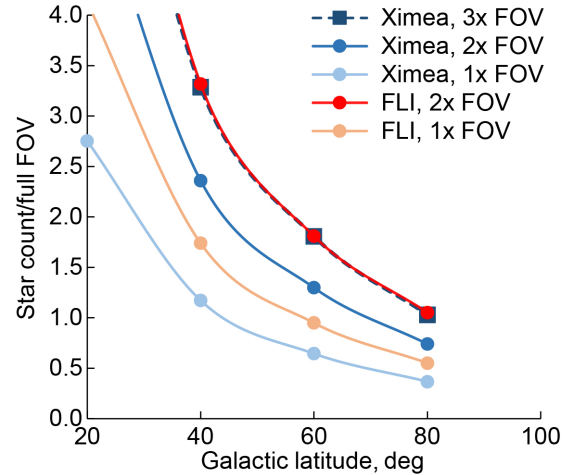


Figure 19.—Predicted FGS star count performance—2 sec. Integration time, FOV as shown in Figure 16, 1σ jitter velocities.

3.1.13 Photometric Analysis Conclusion

Results in Figure 19 show that at least two of the configurations (2x FLI and 3x Ximea) are capable of capturing at least one star at galactic latitudes up to 80° , which is greater than 98 percent of the sky. Additionally those same camera configurations would also yield greater than two stars at galactic latitudes higher than 55° , which is more than 80 percent of the sky. From a mass and power consumption standpoint, the FLI configuration is best, however the use of nonorthogonal angles in the two-camera orientation could become difficult to transform and merge if the FGS must operate at relatively fast frame rates. Current expectations for FGS measurement period is on the order of 60 sec, which should be adequate to accommodate the extra computation, which the FLI configuration may need. Hence, the two-camera FLI configuration is recommended for FGS implementation, if this functionality is to be part of the GHAPS facility.

3.2 Pointing Requirements

In light of the potential pointing bias offset issue, a re-examination of the GHAPS pointing requirements was undertaken in parallel with the FGS trade study. The results yielded modifications to existing requirements and additional new pointing requirements for GHAPS. Some of the key changes included the following:

1. A separation of pointing requirements into short term (jitter) and longer term (bias).
2. WASP and OTA will provide an absolute point error of less than 45 arcsec (3σ).

3. Given a target relative offset (bias offset), GHAPS shall point the mean optical axis of the telescope within 0.1 arcsec (3σ) of commanded position.

Item 2 above indicates the maximum possible bias offset that could be present at Cassegrain focus due to deflections and deformations in the OTA. Item 3 above reflects the long term pointing accuracy needed to meet mission success. Item 3 was derived by a detailed examination of potential science missions

listed in the GHAPS SIDT Report. Therefore, any FGS system will need to measure bias offset to an accuracy of better than 0.1 arcsec.

3.2.1 FGS Measurement Accuracy

An estimate of the FGS measurement accuracy was undertaken based on the configuration recommended in Section 3.1.14. In order to estimate the measurement accuracy, some notional algorithm is needed for computation. The FGS camera

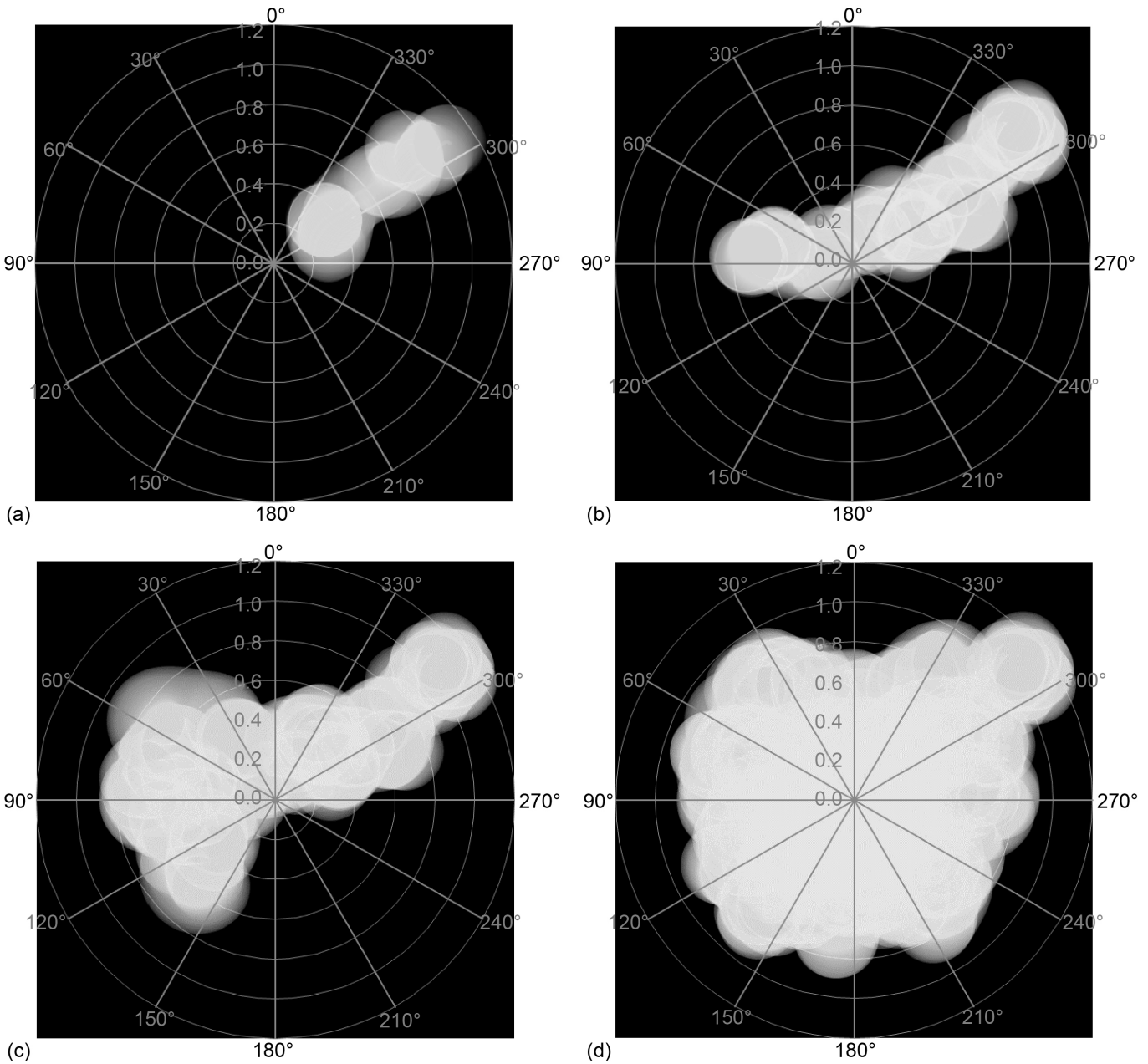


Figure 20.—Synthetic PSF image smear for GHAPS/WASP pointing jitter simulation (magnitude axis is in arcsec)
 (a) GHAPS/WASP simulation PSF jitter, 1 sec. (b) GHAPS/WASP simulation PSF jitter, 5 sec. (c) GHAPS/WASP simulation PSF jitter, 10 sec. (d) GHAPS/WASP simulation PSF jitter, 60 sec.

will need to operate with multiple integration times to avoid saturation effects. Two integration times can be assumed, one optimized for the dimmest stars (approximately 2 sec), and one for bright stars (approximately 1 msec). These images will be combined after acquisition, and adjusted to create a single very high bit depth image with all imageable stars available for FGS algorithm processing. The FGS will utilize a simple center of mass centroid algorithm to estimate star position within the image. The centroiding algorithm accuracy will be susceptible to image jitter. Based on the estimated WASP jitter frequencies and the FGS camera integration time, errors could be significant enough to warrant additional time averaging in software beyond 2 sec to improve accuracy. In this case, the FGS will need to perform additional processing to effectively co-add individual frames to create an extended duration image that can be used for a Lost-In-Space pattern-matching algorithm which determines the FGS FOV in celestial coordinates. Using the WASP jitter simulation as a function of time and a basic model of the star PSF, synthetic time-lapse images of the stars were generated for various integration time from 1 to 60 sec. Some of the time-lapse images are shown in Figure 20.

Using a simple center mass weighted centroiding algorithm, the computed star position was then compared to the cross boresight origin. The results are shown in Figure 21 as the noise equivalent error angle (NEA) for the FGS in arcsec. NEA values were calculated using the process outlined in Liebe, 2001 (Ref. 13). NEA values were computed for two camera configurations with a single star capture (FL400 = 11 μm pixel, Ximea = 4.5 μm pixel), which yields the worst case NEA. Additional star capture improves NEA, and a three-star case is shown for reference. NEA does not represent all sources of error that could contribute to FGS accuracy, but it is the largest inherent error source that cannot be calibrated out or reduced by additional processing. In all cases, the FGS system appears to be capable of delivering better than 0.1 arcsec using accumulated measurement time greater than approximately 10 sec.

3.2.1.1 FGS Alignment Errors

The NEA shown in Figure 21 assumes that the FGS optical components are ideally mounted to the OTA with no misalignment occurring during flight. Gravity and thermal effects are expected to cause deflections in flight at the mounting points for FGS components, however a quantitative analysis that included the OTA and Instrument Deck was unavailable at the time of this trade study. As a means to understand the FGS system misalignment, a notional FGS optical component layout was considered where the FGS pickoff mirror is located along the OTA optical axis at a 45° angle (see Figure 22). The FGS Camera is located approximately 50 mm from the pick-off mirrors centerline. Any FGS band pass filters are built into the camera housing.

Assuming rigid bodies for the pick-off mirror and Camera, the angular and displacement sensitivities were calculated for each component. Results are shown in Table 3.

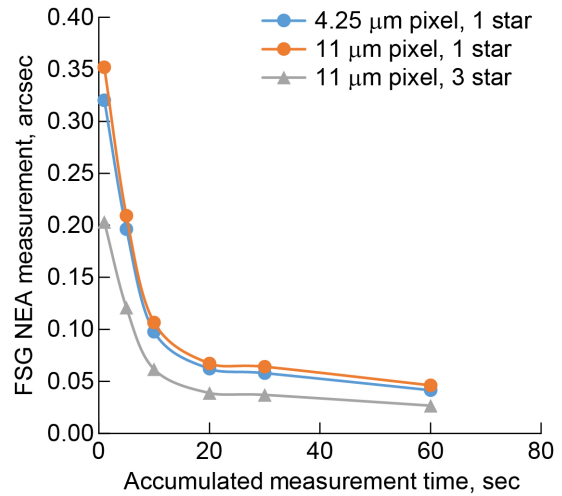


Figure 21.—Estimated FGS Measurement NEA for sCMOS Configurations.

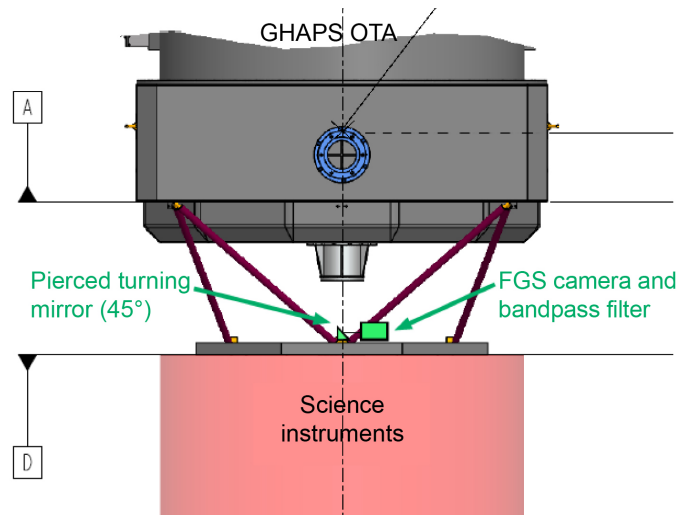


Figure 22.—Notional FGS OPTICS CONFIGURATION (approximate scale for FGS components).

TABLE 3.—FGS OPTICAL COMPONENT MISALIGNMENT SENSITIVITIES

Element	Angular sensitivity	Displacement sensitivity	Comment
Pickoff mirror	3.6 marcsec/arcsec	0.01 arcsec/μm	Rigid body mirror
Camera	N/A	0.015 arcsec/μm	Assumes filter is optically thin.

The misalignment sensitivities are high in some cases. As an example, if a camera displacement of 10 μm occurs during tracking, as much as 0.15 arcsec of misalignment is seen in the FGS FOV, which is beyond the required FGS system performance. The inflight misalignment errors of the FGS optical components cannot be corrected and will contribute directly to the overall system error.

3.3 FGS Implementation

The previous photometric analysis assumed that the GHAPS OTA and Avionics would provide the hardware and software needed for the FGS. As an alternate approach, the possibility of implementing the bias offset measurement capability in the Science Instrument was considered. The GHAPS Science Instrument (SI) is a large high-performance instrument package (200 kg, 1 m^3) that provides the capability to accomplish the GHAPS science mission objectives. The SI developers have the freedom to design a single or multi-instrument package that best meets the science mission objectives. The SI could be modified or completely swapped out for another SI should the project require it for future missions.

Using the SIDT report as a guide for possible science missions, the most likely form that a GHAPS SI will take is either an imaging instrument (focal plane array) or a non-imaging instrument, such as a spectrometer. Imaging instruments will inherently have star imaging capability similar to that needed for the FGS, depending on its FOV. Similarly, almost all conceivable spectrometer-type instruments will also need imaging capability to facilitate continuous spectrometer slit placement. The possibility exists that SI designers could incorporate pointing bias offset measurement capability within the SI without major impacts to the basic SI design.

3.3.1 FGS Versus SI Tradeoffs

A number of design factors were examined to understand the impacts of an SI-based bias offset measurement system compared to the baseline FGS.

3.3.1.1 SI Versus FGS Performance

The key performance measures for bias measurement are detectable stars per FOV and NEA. These factors have been estimated for the recommended FGS configuration and found to be adequate using commercial scientific imagers. Assuming the same hardware components and processing algorithms are available to the SI designers, similar performance should be attainable. For detectable stars per FOV, SI-based systems should have an advantage compared to the FGS. The FGS optical configuration places the pickoff mirror at least 50 mm before

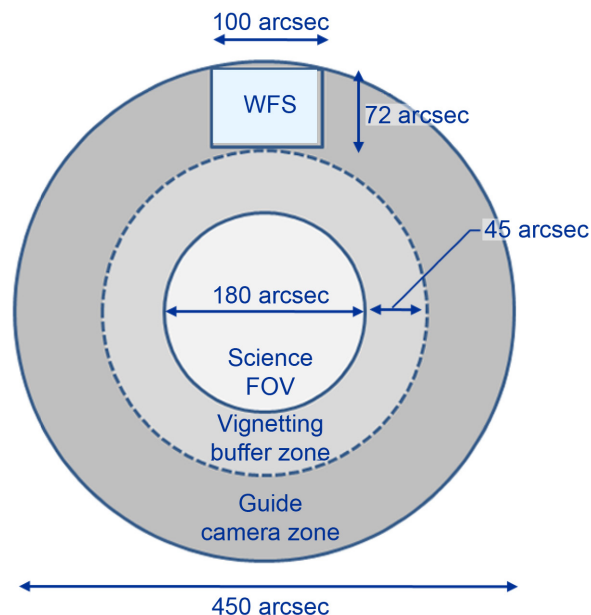


Figure 23.—GHAPS OTA FOVs at Cassegrain focus.

Cassegrain focus. At this point in the optical train, the ray bundle for a point source has an approximate diameter of 44 arcsec. The OTA Science FOV (180 arcsec diameter) must be preserved without any artifacts or vignetting from the FGS pick off mirror. To avoid vignetting any star ray bundle, the pickoff mirror must not encroach on the vignetting buffer zone that exists around the Science FOV, as shown in Figure 23. This limits the available FOV for the FGS to roughly 9.0×10^4 arcsec². In contrast, an SI-based system can be located closer to the focal plane and have fewer restrictions on vignetting keep out zones. In the case of a high-performance SI focal plane array, the same array has the potential to be used for bias offset measurement, in which case the entire FOV outside the SI is available.

NEA is a function of FOV, star centroid error, and the number stars detected. Assuming an SI-based system could have the same components, NEA should be equal to the FGS system or potentially higher since the available FOV could be larger.

The uncorrectable errors that affect the FGS optical components will still be a factor for SI-based systems, however due to the tighter mechanical and thermal coupling of the same components to the desired SI FOV, in-flight misalignment impacts are expected to be reduced. SI-based guider optical components will be located much closer to the SI internal focal planes, such as the SI Science image sensor or Science spectrometer slit, hence misalignment sensitivities are lower. In addition, SI-based guider optical components will likely be mounted to the same optical bench as the SI detectors.

3.3.1.2 SI Versus FGS Size Weight and Power (SWAP)

In the case of a spectrometer-type SI package, a separate SI guider system is needed to ensure slit alignment during observation. The same hardware components needed for FGS will be needed in the SI-based system. It is possible that some of the SI guider components could be smaller in mass due to their location nearer the SI internal focal plane(s), however the difference is only minor. More significant mass differences would exist in the guider camera cooling configuration. All FGS cameras being considered require image sensor cooling to reduce noise and achieve the claimed performance. Cooling takes the form of either dissipating heat via a cooling plate or dedicated cooling fluid lines fixed to the camera. GHAPS will provide the SI package with closed loop capacity of 400 W. Any SI detector is inherently expected to require use of the GHAPS cooling loop to meet the cutting edge science mission objectives. For an SI-based guide system, the designers will be able to internally distribute the cooling loop to those components that need it. In contrast, the FGS system will require additional cooling lines run to multiple cameras. The weight penalty is worse for FGS cameras that require a cooling plate. Therefore, SI-based guider systems are expected to have less mass than FGS concepts.

Due to the optical layout flexibility that SI guiders systems will have, the potential exists that the same FOV covered by 2 or 3 FGS camera could be accomplished with a single SI-based guider camera. In this case, the power consumption would be lower than for the SI-based system. Conversely, if the SI-based system goal is to equal the bias measurement resolution of the proposed FGS, a multiple camera system is more likely. Therefore, the power consumption difference is considered to be zero between FGS and SI-based systems.

The current volume allotted for the SI should be adequate to accommodate an SI-based system. Based on similar balloon payload instruments on the Balloon Observation Platform for Planetary Science (BOPPS) (Ref. 14), which did employ a separate guide camera, the additional volume is well within the allotted volume for the GHAPS SI. Therefore, neither FGS nor SI-based systems should impact the current GHAPS volume constraints.

3.3.1.3 SI Versus FGS Cost and Schedule

FGS Development costs have been estimated to be \$1,500K over 3 years and includes all labor and purchases. The current estimate for the entire SI development is roughly 5 times the FGS. The current FGS concept is driven by satisfying all possible science missions so as to achieving the best possible performance with the least available FOV for guiding. SI developers are expected to optimize their designs to a tighter range of science targets for each observation campaign. This allows SI designers to optimize their SI guider designs in the same way, which could

lead to a less costly configuration compared to the FGS. This design flexibility combined with a larger FOV available for guiding gives the SI-based systems a slight cost advantage.

Requiring the SI to provide its own bias offset measurement capability is not trivial and will impact resources of any contractor. Much of the SI-based guider tasks can be performed in parallel with the SI main instrument development, but regardless the contractor schedule will be impacted. The level of impact is very dependent on the contractor's workforce size and/or experience base.

One area where the SI-based guider development impacts the GHAPS schedule is at system level Assembly Integration and Test (AI&T). With an FGS development schedule scenario, the capability for evaluating bias detection and pointing error will be incorporated in the OTA at an earlier phase. SI-based systems will arrive later in the AI&T process. The project would be without a means to measure system pointing performance until the SI arrives. If any functional issues arise with pointing, the project will have less time to resolve them. To mitigate this risk, GHAPS could develop a simplistic bias measurement system that mimics the SI-based system from an optical standpoint, but without the pure performance of the flight unit. This system could be ready much earlier than the complete SI, and used for OTA AI&T activities that require pointing measurements. The pseudo SI-based guider could be developed with a fraction of the cost estimated for the FGS. Regardless of mitigation, the FGS still has a slight advantage in project schedule.

3.3.1.4 SI Versus FGS Mission Operations Impact

The FGS concept present herein assumes that the SI is not involved in the bias offset measurement or correction process. FGS acquires the images, processes the images to create a single high bit depth image that can be used for Lost-in-Space (LIS) pattern matching, which locates the FGS FOV in celestial coordinates. FGS image processing and LIS computation is carried out in either the existing GHAPS Avionics Computer or a small dedicated FGS computer. The center of the FGS FOV is then compared to the WASP star tracker FOV to obtain the bias offset, and the bias offset is applied to the WASP pointing system so that the desired science target falls within the center of the OTA Science FOV. In an SI-based guider system, the SI will be responsible for the image acquisition, image processing, and possibly the pointing correction process. This has the potential to impact the operations concept during GHAPS observation periods.

It should be noted that envisioned SI-based systems that perform LIS calculations will use a seeded data set. Instead of requiring the SI to compare its FOV to an entire magnitude 16 star catalog of the sky, current WASP star tracker FOV coordinates are provided to the SI, and the SI LIS calculation need only operate on this subset of the full star catalog.

Three versions of SI-based guider involvement were considered which range from fully automated to a partial manual system. They are described in Table 4. If we consider the FGS operations concept as the baseline, the three possible SI-based guider options can be compared for their impact on GHAPS operations during observation times.

The FSG Automatic concept is most similar to the FGS baseline in terms of operations. A bias offset is calculated and passed to the WASP for pointing correction. The SI Automatic concept calculates the offset in the same manner but assumes the SI has a Fine Steering Mirror (FSM) as part of its optical train that can redirect the SI FOV the required amount so that the science target falls in the center of the Science FOV. The SI Automatic concept comes about due to the expectation that many science missions require precise short term (jitter) positioning, below even the 1 arcsec provided by WASP. The most common solution for better jitter performance is a FSM. The FSM will operate at high speeds, and depending on its FOV, could be used as a means to apply the long-term (bias) offset that occurs during observations. The SI Automatic bias configuration could have a somewhat limited correction range, since the FSM will likely induce additional aberrations that could detract from the near diffraction limited optical performance goal. A more detailed optical analysis with the complete OTA and SI is needed to estimate this effect.

The semiautomatic version emphasizes a concept where minimal SI processing is needed and unburdens the SI from some image processing and all of the LIS computation. A single or set of high bit depth images are downlinked to the ground, additional image processing and the LIS calculation is carried out on the ground. The offset is uplinked to the WASP and corrected. This operational scenario requires downlink and uplink capability for the balloon platform. Depending on mission locations and flight profiles, uplink and downlink capability may be significantly restricted, making it more desirable to have a system that is autonomous.

Once the bias has been initially corrected, the update during observation could be carried out automatically, if the SI simply

sends a guide star position change parameter to the WASP. This is far less computationally intensive than LIS computation. The semiautomatic process lends itself to situations where the camera captures only a single star in the FOV. Automated LIS processing requires at least 2 stars in the FOV. When only 1 star is visible, some manual intervention is needed to determine its identity and celestial coordinates before it can be used for bias offset measurements during tracking observations.

Even the FGS will require manual intervention if FOV star count is fewer than two stars, therefore the SI-based and FGS type systems are essentially equal in terms of negative impact on GHAPS operations concepts.

3.4 Implementation Recommendation

A number of factors have been taken into consideration when determining the optimum implementation for measuring bias offset. Table 5 summarizes the advantages and disadvantages of FGS and SI-based systems.

There is understandably a desire to divorce the bias detection capability from the SI, so that the GHAPS system is completely self-sufficient in terms of pointing correction. It simplifies the interface to the SI and does provide the capability for GHAPS to perform WFS correction without SI involvement. However, with exception of schedule impact, an SI-based guider is expected to have equal or better characteristics for all factors being considered. Of particular concern is the uncorrectable errors that come about from guide system optical component deflection. Using the misalignment sensitivities estimated for the FGS, even a very small deflection exceeds the measurement accuracy requirement. The SI-based systems will inherently have lower sensitivities to deflection, and is the best implementation from an engineering and performance standpoint. In general, having the full design trade space in the hands of the SI developer makes for an optimized bias measurement system that is not over designed or underperforming.

The main drawback to a SI-based system is that it burdens the SI developer with additional work and cost. Any additional

TABLE 4.—SI-BASED GUIDER SYSTEM IMPACTS ON GHAPS OPERATIONS CONCEPTS.

SI-based system	Bias measurement and correction process	Operations impact (compared to baseline FGS)
SI automatic	SI calculates offset automatically using seeded LIS algorithm and SI actuates.	<i>Lower than baseline.</i> SI corrects bias with Fine Steering Mirror.
FGS automatic	SI calculates offset automatically using seeded LIS algorithm and WASP actuates.	<i>Same as baseline FGS.</i> Fully automated calculation, WASP corrects bias.
Semiautomatic	SI calculates offset semiautomatically for guide stars without LIS, SI downlinks FOV image/data at target, offset calculated manually, uplinked, and WASP actuates.	<i>More than baseline.</i> Automatic calculation when on bright guide star. Manual calculation when at target location.

TABLE 5.—FGS VERSYS SI-BASED GUIDER COMPARISON SUMMARY

	Facility guider subsystem (FGS)	Science instrument (SI-based) guider	Comment
SWAP (size, weight, and power)	Worse. (FGS camera cold plate)	Better (Cooling built into SI)	No need for additional cooling lines in SI-based system.
Daytime star performance	1 star over 98% of sky 2 stars over 80% of sky	Equal or better	SI-based systems should have more FOV available than FGS.
Bias offset measurement accuracy	Good	Better	SI Guider will have significantly lower uncorrectable bias offset.
Cost	Highest	Equal or lower (Regardless, SI will have to have this functionality to meet science jitter pointing requirements)	Optimization of SI Guider should allow for possibility of lower cost components. (subsequent SIs may have increased cost due to guider mandatory inclusion)
Operations Impact	Minimal with auto LIS	Minimal with auto LIS (Potentially lower with FSM within SI)	Both systems impact con-ops when FOV contains only 1 star.
AI&T Impact Risk	Good (GHAPS will have bias, pointing, and PSF functional checkouts without need for SI.)	Worse (GHAPS relies on SI for functional checkouts of bias, pointing, and PSF.)	Risk can be mitigated by designing functionally equivalent GSE that can be used earlier in AI&T flow. Additional cost though.

future SI for GHAPS must also provide the same form of bias offset measurement, ultimately impacting long-term program costs.

Most of the candidate science missions discussed in the SIDT Report will require active pointing correction for jitter performance better than WASP can deliver. The majority of jitter compensation solutions will require some form of guider-like imaging capability within the SI. SI designers should be able to augment these systems to perform the bias correction as well. This configuration tends to be the most prevalent in similar class observatory systems. For these reasons an SI-based bias offset measurement system is recommended for GHAPS implementation, and the project should allow SI developers options in the level of automation for system operations.

References

- Zombeck, M., "Handbook of Space Astronomy and Astrophysics, 2nd Edition," Cambridge University Press, 1982.
- Pecaut, M.J.; Mamajek, E.E., "Intrinsic Colors, Temperatures, and Bolometric Corrections of Pre-main-sequence Stars," The Astrophysical Journal Supplement, Vol. 208, Issue 1, 2013.
- Jim, K., Gibson, B., Pier, E., "Daytime Sky Brightness Modeling of Haleakala along the GEO Belt," Proceedings of the Advanced Maui Optical and Space Surveillance Technologies Conference, 2012, id 68.
- Chanover, et al., "Results from the Science Instrument Definition Team for the Gondola for High Altitude Planetary Science Project," American Astronomical Society, DPS meeting #48, id.123.31, 2016.
- Esplin R. et al., "SABER Instrument Overview," Proc. SPIE Vol. 2268, pp. 207-217, 1994.
- Vollmerhausen, R.H., et al "Night illumination in the near-IR and short-wave infrared spectral bands and the potential for silicon and indium-gallium-arsenide imagers to perform night targeting," SPIE Optical Engineering, Vol. 52, id 043202 (2013).
- Noll S., et al, "An atmospheric radiation model for Cerro Paranal," Astronomy & Astrophysics, Vol. 543, id.A92, 23 pp. 2012.
- Vollath, D., "Automatic Focusing by Correlated Methods", J. Microsc., 147, pp. 279-288, 1987.
- Feruson, H., et al., "Image Quality Guidelines, NGST Monograph No. 7," Space Telescope Science Institute, 2001.
- Ledrew, G., "The Real Starry Sky," Journal of the Royal Astronomical Society of Canada. 95: 32, Feb. 2001.
- Stellar classification, Wikipedia, https://en.wikipedia.org/wiki/Stellar_classification, 2020.
- Houdashelt, M.L.; Bell, R.A.; Sweigart, A.V., "Improved Color-Temperature Relations and Bolometric Corrections for Cool Stars," The Astronomical Journal, Vol. 119, Issue 3, pp. 1448-1469, 2000.
- Liebe, C.C., "Accuracy Performance of Star Trackers – A Tutorial", IEEE Transactions On Aerospace and Electronic Systems Vol. 38, No. 2, April 2002.
- Dankanich J.W., et al., "Planetary Balloon-Based Science Platform Evaluation and Program Implementation—Final Report," NASA/TM—2016-218870, 2016.

